

# LENGTH SCALES AND TURBULENT PROPERTIES OF MAGNETIC FIELDS IN SIMULATED GALAXY CLUSTERS

HILARY EGAN<sup>1</sup>, BRIAN W. O'SHEA<sup>2</sup>, ERIC HALLMAN<sup>3</sup>, JACK BURNS<sup>1</sup>, HAO XU<sup>4</sup>, DAVID COLLINS<sup>5</sup>, HUI LI<sup>6</sup>, AND MICHAEL L. NORMAN<sup>4</sup>

<sup>1</sup>Center for Astrophysics and Space Astronomy, Department of Astrophysical and Planetary Sciences, University of Colorado, Boulder, CO 80309, USA  
[Hilary.Egan@colorado.edu](mailto:Hilary.Egan@colorado.edu)

<sup>2</sup>Department of Computational Mathematics, Science and Engineering, Department of Physics and Astronomy, and National Superconducting Cyclotron Laboratory, Michigan State University, East Lansing, MI 48824, USA [oshea@msu.edu](mailto:oshea@msu.edu)

<sup>3</sup>Tech-X Corporation, Boulder, CO 80303, USA

<sup>4</sup>University of California at San Diego, La Jolla, CA 92093, USA

<sup>5</sup>Florida State University, Tallahassee, FL 32306, USA and

<sup>6</sup>Los Alamos National Laboratory, Los Alamos, NM 87545, USA

*Draft version August 4, 2016*

## ABSTRACT

Additional physics beyond standard hydrodynamics is needed to fully model the intracluster medium (ICM); however, as we move to more sophisticated models, it is critical to consider the role of magnetic fields and the way the fluid approximation breaks down. This paper represents a first step towards developing a self-consistent model of the ICM by characterizing the statistical properties of magnetic fields in cosmological simulations of galaxy clusters. We find that plasma conditions are largely homogeneous across a range of cluster masses and relaxation states. We also find that the magnetic field length scales are resolution dependent and not based on any specific physical process. Energy transfer mechanisms and scales are also identified, and imply the existence of small scale dynamo action. The scales of the small scale dynamo are resolution-limited and are likely to be driven by numerical resistivity and viscosity.

*Subject headings:* galaxy clusters: plasma – galaxy clusters: intracluster medium – magnetohydrodynamics

## 1. INTRODUCTION

Simulations of galaxy clusters have made rapid advances in the past few years, and match observations of galaxy clusters in a wide variety of ways – generally, observationally determined density, temperature, and entropy profiles of clusters are reproduced in simulations, at least outside the central regions (see, e.g., Hallman et al. 2006; Nagai 2006; Borgani & Kravtsov 2009). This matching indicates that the intracluster medium (ICM) properties, at least in terms of the integrated observables in the cluster volume, are largely driven by the gravitational potential of the dark matter halo in which the ICM plasma resides, and that simple hydrodynamics and gravity can account for the general behavior of the intracluster plasma (Burns et al. 2010).

There are some observational incongruities regarding the intracluster medium, however – in terms of bulk quantities, simulations do a poor job of matching the properties of the intracluster medium in cluster cores, particularly in cool-core clusters (e.g., Skory et al. 2013). Also, there are some observational features, such as cluster cold fronts (see, e.g., Markevitch & Vikhlinin 2007; Vikhlinin & Markevitch 2002), that are difficult to explain with our standard models and require more sophisticated plasma physics to understand (e.g., ZuHone et al. 2015; Werner et al. 2015).

More broadly, it is clear that additional physics is needed to model the intracluster medium (ICM): synchrotron radiation from radio relics and radio halos indicate that there is acceleration of charged particles to relativistic speeds by some combination of the first- and second-order Fermi processes (Clarke & Ensslin 2006; Giacintucci et al. 2009; van Weeren et al. 2010; Skillman et al. 2013; Datta et al. 2014). This also requires the presence of magnetic fields. Similarly, other observations, such as Faraday rotation measures of background light passing through the ICM (Bonafede et al. 2010a; Mur-

gia et al. 2004), show that magnetic fields are ubiquitous in clusters, both in the cluster core and in the outskirts of clusters (Carilli & Taylor 2002; Clarke & Ensslin 2006; Burns et al. 1992). While magnetic fields are typically dynamically unimportant (plasma  $\beta$  values estimated from observation are  $\gg 1$  in essentially all of the cluster outside of AGN jets and, perhaps, jet-driven bubbles), they are essential to reproducing these types of observations.

Estimates of the Reynolds number ( $Re$ ), magnetic Reynolds number ( $R_M$ ), and Prandtl number ( $Pr$ ) suggest that a small scale dynamo process will work to amplify a small seed magnetic field, possibly to levels observed in the ICM (Subramanian et al. 2006). As has been argued in the recent work by Miniati (2014, 2015), the plasma in galaxy clusters has an extremely high Reynolds number ( $Re \equiv UL/\nu$ , having effectively zero viscosity), and thus must develop Kolmogorov-like turbulence very rapidly. The ICM also satisfies  $\eta \ll \nu$  (Brandenburg & Subramanian 2005; Subramanian et al. 2006), leading to large Prandtl numbers ( $Pr \equiv \nu/\eta \gg 1$ ) and magnetic Reynolds numbers ( $R_M \equiv UL/\eta \gg Re$ ).

Limitations in current simulation capabilities mean that it is infeasible to simulate fluids with such large Reynolds and Prandtl numbers, as both ideal viscosity and resistivity are much smaller than numerical viscosity and resistivity. Furthermore, the highest Reynolds numbers are only achieved in turbulent box simulations; cosmological scale simulations are further limited ( $Re \sim 500 - 1000$ ). These conditions drastically change the nature of any small scale dynamo, if indeed they are even capable of exciting one.

There are various physical processes that have been modeled in clusters in recent years – thermal conduction, viscosity, and subgrid turbulence – that are typically treated as independent (e.g., Smith et al. 2013; Brügggen et al. 2009), but are all critically dependent on the behavior of the magnetic field and its interaction with the plasma at both observable

scales and below. As a result, a truly self-consistent model of the intracluster plasma must treat all of these phenomena, and others as well, as manifestations of local plasma properties. The magnetic field evolution will thus depend on the effects of the subgrid properties and the subgrid properties must be influenced by the local magnetic field.

Making such a model is a significant theoretical challenge, and due to practical constraints it is beyond the scope of cosmological simulations of galaxy cluster formation and evolution – simulations that resolve all relevant scales in galaxy clusters, from cosmological scales down to the turbulent dissipation scale, are computationally unfeasible. However, an important first step is to characterize the statistical properties of magnetic fields in cosmological simulations of galaxy clusters, which will serve to motivate more sophisticated plasma modeling at a later date. We must examine how and if amplification is taking place and what signatures it is imparting on the magnetic field, as well as the numeric and model-dependent resistive features. Although such processes have been examined in isolation in the form of turbulent box simulations, it is also necessary to compare to full cosmological simulations with the effects of merger driven turbulence and strong large scale density gradients.

Our goal is to analyze the magnetic field amplification signatures of a set of 12 high-resolution cosmological magnetohydrodynamical (MHD) simulations of galaxy clusters from Xu et al. (2009, 2010, 2011, 2012), as they relate to the numerical effects arising from resolution limitations. We generally focus on the statistical properties of the cluster turbulence and magnetic fields as well as the differences between clusters that are morphologically relaxed in X-ray observations, and those that are unrelaxed (i.e., that display evidence of recent mergers).

This paper is organized as follows. In Section 2 we discuss the simulation setup and the general characteristics of our cluster sample. In Section 3 we present our main results including a selection of global cluster properties (Sec. 3.1), identification of the scale lengths present in the plasma (3.3.1), and energetic properties of the plasma (3.3.1, 3.3.2). We discuss these results in the larger context of ICM plasma simulations in Section 4. Finally, Section 5 contains a summary of our findings.

## 2. METHODS

### 2.1. Simulation

The simulations we analyze were previously studied in Xu et al. (2012). They were run using the cosmological code ENZO (Bryan et al. 2014), with the ENZO+MHD module (Collins et al. 2010). The cosmological model chosen was a  $\Lambda$ CDM model with cosmological parameters  $h = 0.73$ ,  $\Omega_m = 0.27$ ,  $\Omega_b = 0.044$ ,  $\Omega_\Lambda = 0.73$ , and  $\sigma_8 = 0.77$ .

To simulate the clusters, eleven boxes with different random initial seeds were run. The simulations were evolved from  $z = 30$  to  $z = 0$ . An adiabatic equation of state was used ( $\gamma = 5/3$ ), and no additional physics such as radiative cooling or star formation was used. The magnetic field was injected using the magnetic tower model (Xu et al. 2008; Li et al. 2006) at  $z = 3$ . The tower model is designed to represent the large scale effects of a magnetic energy dominated AGN jet, and the total energy injected ( $\sim 6 \times 10^{59}$  erg over  $\sim 30$  Myr) is similar to the energy input from a moderately powerful AGN. One cluster was run twice with magnetic field being injected in a different protocluster during each run.

**Table 1**  
Cluster Sample

$R_{200}$ (Mpc)	$M_{200}$ ( $M_\odot \times 10^{14}$ )	Temperature (KeV)	Relaxation
4.08	18.01	9.04	R †
3.45	11.95	6.80	R
3.01	7.53	5.38	R
3.00	5.94	3.80	R
2.34	2.97	2.74	R
1.81	1.44	1.65	R
2.74	7.52	5.55	U*
2.34	7.18	5.51	U*
3.30	8.75	5.88	U
2.68	6.99	5.43	U
3.16	8.44	5.75	U
2.99	5.93	4.39	U

**Note.** — Cluster properties for the full sample of clusters.  $R_{200}$  and  $M_{200}$  are calculated with respect to the critical density using spheres centered via iterative center of mass calculations. The temperature is calculated using the virial mass-temperature relationship ( $k_B T = (8.2 \text{ keV})(M_{200}/10^{15} M_\odot)^{2/3}$ , at  $z = 0$  (Voit 2005)), and relaxation is defined by having more or less than half the final mass of the cluster accumulated by  $z = 0.5$ . Asterisks indicate that the two clusters are the same final cluster, but the magnetic field was injected into separate proto-clusters. † indicates that this cluster was resimulated at a higher resolution.

Each cluster was simulated in a  $(256 h^{-1} \text{ Mpc})^3$  box with a  $128^3$  root grid. Two levels of static nested grids were used in the Lagrangian region where the cluster is formed such that the dark matter particle resolution is  $1.07 \times 10^7 M_\odot$ . A maximum of eight levels of refinement were also applied in a ( $\sim 50 \text{ Mpc}$ )<sup>3</sup> box centered on the location the galaxy cluster forms which combine to give a maximum resolution of  $7.81 \text{ kpc } h^{-1}$ . One cluster (marked in Table 1) was simulated again with an additional level of refinement for a maximum resolution of  $3.91 \text{ kpc } h^{-1}$ . The refinement is based on the baryon and dark matter overdensity during the course of cluster formation, and after the magnetic field is injected, all regions where the magnetic field strength is greater than  $5 \times 10^{-8} \text{ G}$  are refined to the highest level. On average, 90–95% of the cells within the virial radius of the cluster are refined at the highest level.

### 2.2. Cluster Sample

From our simulations we gather a sample of 12 total clusters, with 2 clusters having the same initial conditions but different magnetic field injection sites. The clusters cover a range of masses from  $(1.44 \times 10^{14} - 1.8 \times 10^{15} M_\odot)$ . We separate the sample into two groups (relaxed and unrelaxed) based on whether they have accumulated more than half of their final mass by a redshift of  $z = 0.5$  as described by Xu et al. (2011). A full summary of the cluster properties is given in Table 1. A star indicates that the clusters are the same final cluster, but the magnetic fields were injected into separate proto-clusters.

Figure 1 shows a sample of two clusters, a relaxed and an unrelaxed cluster, with velocity and magnetic field streamlines for a thin slice overplotted.

## 3. RESULTS

### 3.1. Global Magnetic Field Properties

#### 3.1.1. Profiles

One inherent difficulty in simulating clusters is the extreme range in scales from the centers of clusters to their outskirts. Baryon overdensity typically changes over several orders of magnitude (as seen in Figure 2), which can influence many properties that affect the turbulent state of the plasma. As such, for much of the following analysis we break down the quantities by baryon overdensity or radius from the center of

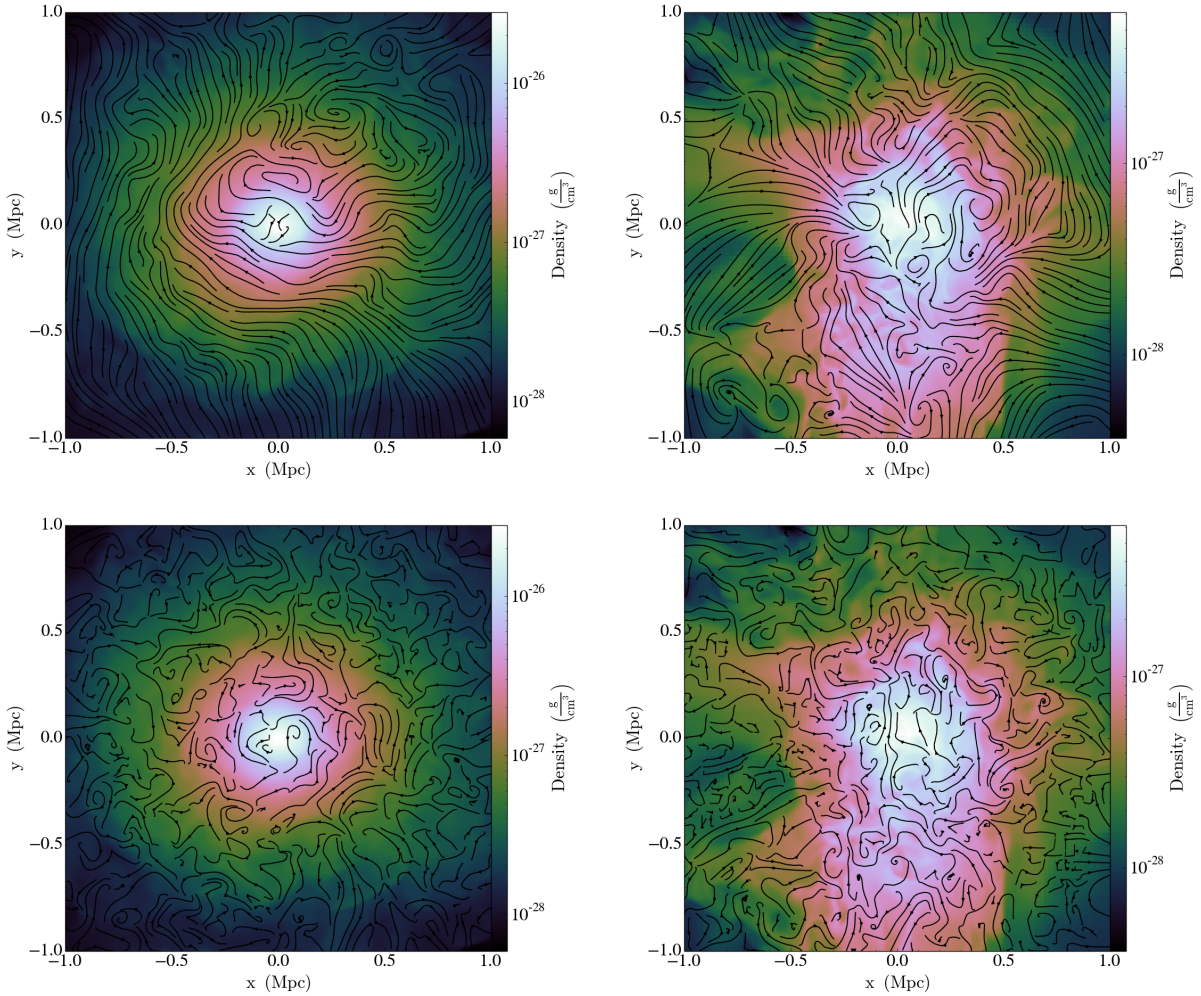


**Figure 1.** Streamlines for velocity (*top*) and magnetic field (*bottom*) plotted over density for a relaxed (*left*) and an unrelaxed (*right*) cluster. Note that while the velocity substructure shows a clear difference between relaxation states, the magnetic field structure appears comparably tangled in both cases.

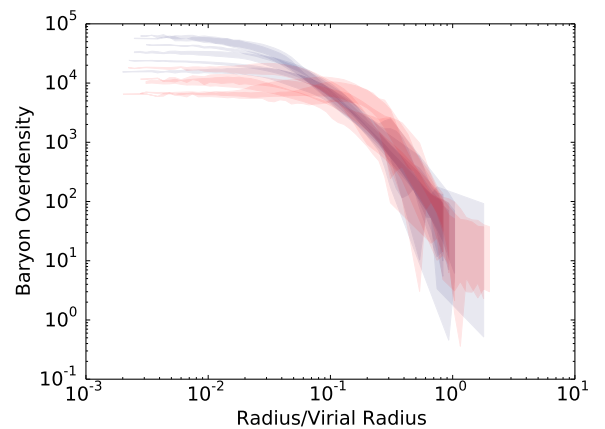
This figure, and some of the following analysis was completed with the aid of open source, volumetric data analysis package, yt (Turk et al. 2011).

the cluster.

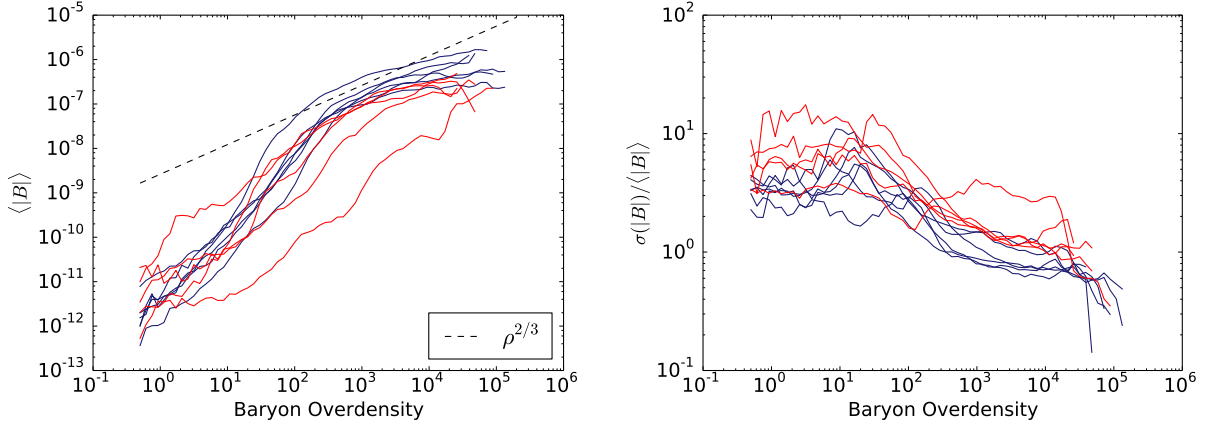
As shown in Figure 3, the magnetic field is not amplified uniformly throughout the cluster. If flux-freezing conditions were completely satisfied and the collapse were completely spherical, the magnetic field magnitude would be proportional to  $\rho^{2/3}$ ; however, this is only true at baryon overdensities greater than  $10^2 - 10^3$  or radii less than roughly half the virial radius of the cluster. This behavior is consistent across relaxed and unrelaxed clusters, although there is one unrelaxed cluster that does not get amplified to the  $\rho^{2/3}$  level at all. This is the least massive cluster, and it is likely that it was injected with too large of a magnetic field for the size of the cluster.

Figure 3 shows the standard deviation around the mean of the magnetic field magnitude shown in Figure 3. In general the scatter in quantities rises as the overdensity falls, indicating that conditions vary more widely at cluster outskirts. Additionally, the variance is generally larger for the unrelaxed clusters.

Plasma  $\beta$  (defined as  $\beta = \frac{P_{\text{thermal}}}{P_{\text{mag}}} = \frac{nk_B T}{B^2/(2\mu_0)}$ ) measures the dynamical importance of the magnetic field pressure. Although



**Figure 2.** Volume-averaged baryon overdensity measured in spherical shells as a function of radius for all clusters. Color indicates relaxation state, where *red* is unrelaxed and *blue* is relaxed. Shaded regions show one standard deviation above and below the mean. This figure may be used as a point of reference for where in the cluster typical baryon overdensities can be found, as used in Figures 3 and 4.



**Figure 3.** Volume-averaged magnetic field magnitude versus baryon overdensity for relaxed and unrelaxed clusters. Red signifies unrelaxed clusters while blue indicates relaxed, with one line per cluster. *Left:* Mean value of magnetic field magnitude, *Right:* variance of the magnetic field magnitude at a given baryon overdensity divided by the mean value of magnetic field magnitude. The dashed line in the left figure shows  $B \propto \rho^{2/3}$ .

these values are typically much greater than 1, the exact distribution varies substantially from cluster to cluster. Figure 4 shows a selection of 2D gas mass-weighted histograms of  $\beta$  vs baryon overdensity, with one panel per cluster. In general these distributions are centered around plasma betas of  $\sim 10^2 - 10^3$  and baryon overdensities of  $\sim 10^3 - 10^4$ ; however, a few clusters have substantial gas mass in tails extending to much higher plasma betas. These can likely be attributed to infalling clumps of gas that have not yet been magnetized.

### 3.2. Scale Lengths

In this section we discuss a variety of scale lengths present in the plasma (Jeans length, characteristic resistive length, and autocorrelation length) as compared to the cell size. The comparison of these scale lengths with the cell size can give insight into the interaction of small scale turbulence with numerical effects due to finite resolution.

#### 3.2.1. Jeans Length

The Jeans length

$$\lambda_J = \sqrt{\frac{15k_B T}{4\pi G \mu \rho}} \quad (1)$$

is the critical length below which a self-gravitating cloud of gas will collapse. Figure 5 shows the mean Jeans length as a function of baryon overdensity, and the mean cell size normalized Jeans length. As these simulations are adiabatic, the direct  $\lambda_{J-\rho}$  relation is a straightforward power law; however, as the adaptive mesh does not resolve every cell in the cluster to the highest level, the  $\lambda_J/\Delta x-\rho$  relation is not an exact power law. Despite this, we always resolve the local Jeans length by at least 40 grid cells, and occasionally resolving it by up to a few hundred.

Federrath et al. (2011) find that the Jeans length must be resolved by at least 30 cells to see dynamo action, and without increased resolution most of the amplification will still be due to compressive forces. Our simulations do exceed this minimum threshold so we may expect to see some dynamo action, but much of the amplification may still be due to compression.

#### 3.2.2. Resistive Length

As mentioned in Section 2, these simulations were refined on both a density and a resistive length based criterion. In Figure 6 we show the mean characteristic resistive length

$$L_R = |B|/|\nabla \times B| \quad (2)$$

and the resistive length divided by the cell size as a function of baryon overdensity. As discussed in Xu et al. (2011), it was critical to also refine based on resistive length in order to achieve even modest levels of magnetic field amplification.

Despite a wide variety of cluster relaxation states and physical conditions, the clusters have very similar resistive lengths as a function of baryon overdensity. In general, there are values of  $\sim 100$  kpc at cluster outskirts and values of  $\sim 10$  kpc at cluster centers, with steep transition happening around baryon overdensities of  $10^2 - 10^3$  (radii of  $0.1 - 0.5 R_{vir}$ ) for most of clusters. As enforced by the refinement criterion,  $L_R/(\Delta x)$  maxes out for most of the clusters at just over one.

Note that the resistive MHD equations are not actually being solved here;  $L_R$  is the "characteristic" local resistive length, and the actual resistive dissipation scale will be much smaller. The sharp floor of the resistive length function is indicative of the limitations in simulation spatial resolution, not of a physical process. This gives some indication of where in the cluster we will see the effects of a finite numerical resistivity directly affecting the magnetic field properties.

#### 3.2.3. Correlation Length

Rotation measure observations find that the cluster magnetic field is patchy, and turbulent down to scales of 10 kpc - 100 pc (Feretti et al. 1995; Bonafede et al. 2010b). Additionally, many observations are interpreted in light of a single scale model where the magnetic field is assumed to be composed of uniform cells of size  $\Lambda_c$  with random orientation (Lawler & Dennison 1982). This produces a Gaussian distribution of patchy magnetic field with zero mean and dispersion  $\sigma_{RM}$ . Murgia et al. (2004) find that using the autocorrelation length as a proxy for  $\Lambda_c$  produces the closest matching  $\sigma_{RM}$  profiles. As our simulations have a maximum resolution of 10 kpc, it is unlikely that field alignment is driven by the same processes at small scales. As one means of addressing the magnetic field spatial distribution in our simulated clusters, we examine the magnetic field autocorrelation length in the intracluster medium. The autocorrelation length is defined

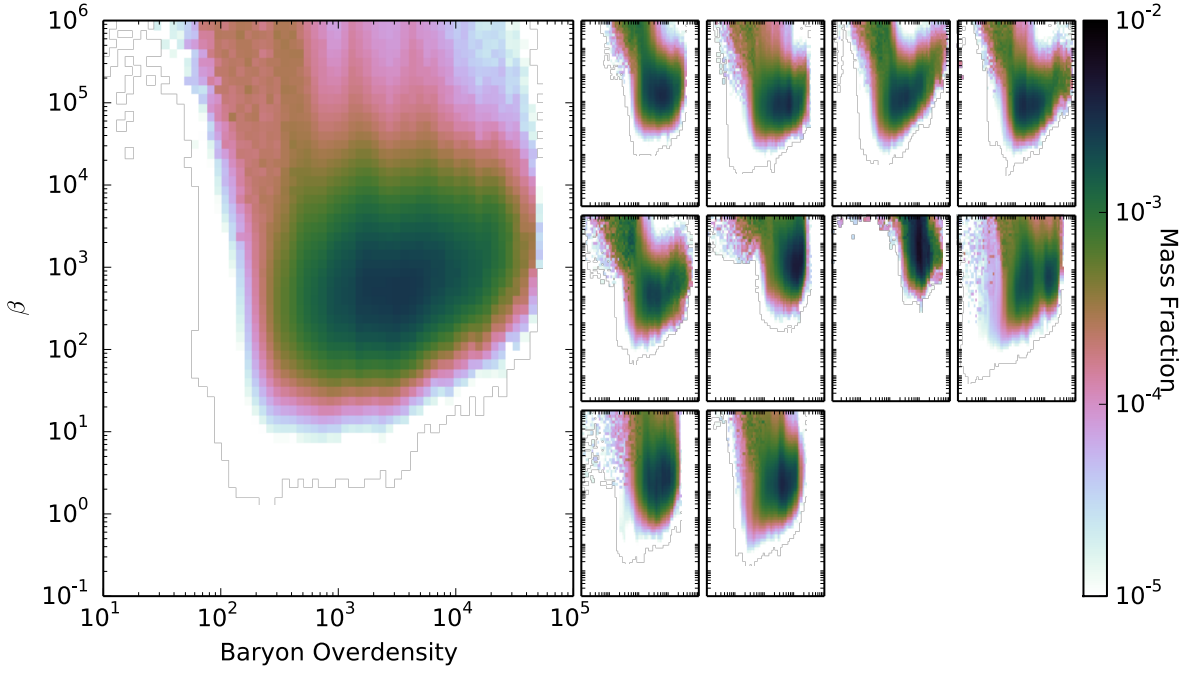


**Figure 4.** 2D gas mass-weighted histogram of plasma beta vs. baryon overdensity. Each panel is a separate cluster with the letters indicating relaxed (*R*) or unrelaxed (*U*). All panels have the same range of baryon overdensity and plasma beta, and the total gas mass is normalized to 1 for direct comparison.

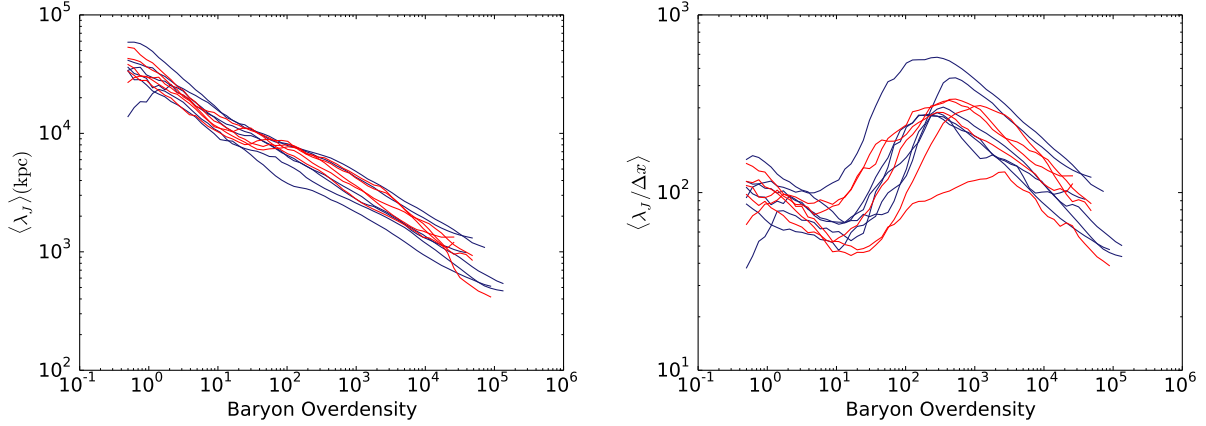


**Figure 5.** Volume-averaged Jeans length versus baryon overdensity for relaxed and unrelaxed clusters. Red signifies unrelaxed clusters while blue indicates relaxed, with one line per cluster. *Left:* Mean value of Jeans length, *Right:* Mean value of Jeans length divided by cell size.

as

$$\lambda_{B_z} = \frac{\int_0^\infty \langle B_z(\vec{x}) B_z(\vec{x} + \vec{\ell}) \rangle d\ell}{\langle B_z(r)^2 \rangle} \quad (3)$$

To calculate the autocorrelation function, pairs of points were picked such that the distance between them falls within a given range of  $\ell$ . We then find the average of  $B_z(\vec{x})B_z(\vec{x} + \vec{\ell})$  for all the pairs of points within the bin. The results are insensitive to the choice of magnetic field orientation used; for brevity, we show only  $B_z$ .

A global autocorrelation function is of limited use due to its contamination by phenomena such as structure in large scale density distributions, the cluster gravitational potential, and bulk flows. As such we show the autocorrelation function separately for a several spherical shells through the cluster.

Figure 7 shows the autocorrelation functions plotted for every cluster with each shell in a different panel, and the colors indicating relaxation state. We find that the magnetic field is more correlated closer to the cluster center; however, cells are not guaranteed to be at maximum resolution at the outskirts of the cluster which may influence the observed autocorrelation. After normalizing for average magnetic field magnitude, relaxed clusters have greater degrees of autocorrelation than unrelaxed clusters, particularly in cluster centers. The turnover occurs at roughly 80 kpc for both relaxed and unrelaxed clusters.

### 3.3. Energetics

Here we discuss energy and energy transfer as a function of scale; both of these measures can provide key insights into the processes acting to amplify the magnetic field.

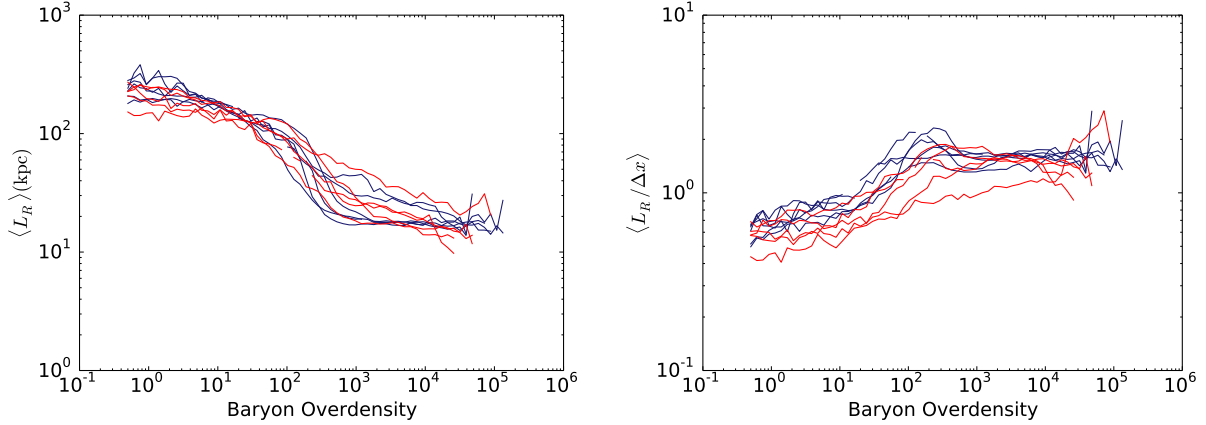


**Figure 6.** Volume-averaged characteristic resistive length versus baryon overdensity for relaxed and unrelaxed clusters. Red signifies unrelaxed clusters while blue indicates relaxed, with one line per cluster. *Left:* Mean value of resistive length, *Right:* Mean value of resistive length divided by cell size.

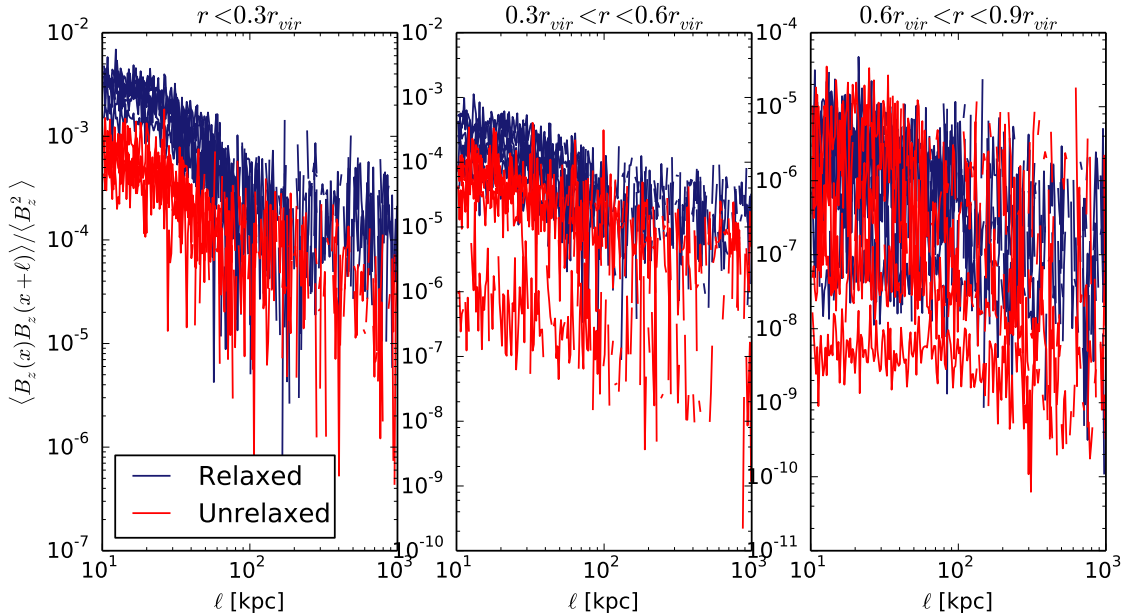


**Figure 7.** Magnetic field autocorrelation function calculated in spherical shells. Each panel shows one spherical shell with a line corresponding to a single cluster. Blue lines indicate relaxed clusters, while red lines indicate unrelaxed clusters. Higher numbers indicate a greater degree of correlation.

### 3.3.1. Structure Functions

Magnetic field amplification processes will impart structure on the magnetic field power spectra, particularly in the inertial range, while numerical effects are likely to dominate at small scales. As in Section we work around this limitation imposed by global cluster structure by examining structure functions of the kinetic energy and magnetic field in spherical shells. The structure function of a quantity  $A(\vec{x})$  of order  $p$  takes the form

$$S_p(l) = \langle |A(\vec{x}) - A(\vec{x} + \vec{d}\vec{x})|^p \rangle \quad (4)$$

We look at exclusively functions of order  $p = 2$  because a power spectrum with scaling index  $\alpha$  has a second order structure function with scaling index  $l = -\alpha - 1$ . For pure Kolmogorov turbulence this corresponds to  $\alpha = -5/3$  and  $l = 2/3$ .

To calculate the structure functions we randomly selected pairs of points with separation  $l$ , uniformly distributed within a thick spherical shell centered on the densest cell in the simulated cluster. The quantity  $|A(\vec{x}) - A(\vec{x} + l)|^2$  is then calculated for each point pair and is averaged over bins in  $l$ . 62,500 point pairs were found for 250  $l$  bins with 250 points per bin. The total number of points was chosen to be large but not over-sample the central region in any cluster. We note that, within reason, the result is robust to the choice of number of points and bins.

In Figure 8 we plot the momentum structure function for each of the three spherical shells. At the center of the clusters ( $r < 0.3R_{vir}$ ) nearly all clusters show some inertial range from  $\sim 80$ –900 kpc. The inertial range has a slope of  $S_2 \sim l^{2/3}$ , typical of incompressible Kolmogorov turbulence. In the middle shell ( $0.3R_{vir} < r < 0.6R_{vir}$ ) only a few of the more massive

clusters show any sort of inertial range. At the largest radii ( $0.6R_{vir} < r < 0.9R_{vir}$ ) no clusters show any sort of inertial range. It is also possible that the compressible nature of the turbulence makes the scaling behave more like supersonic turbulence, in which case one would expect a steeper slope in the inertial range (Kritsuk et al. 2007). We note that the smaller wavenumbers ( $l < 30\Delta x = 300$  kpc) may be contaminated by numerical effects (Kitsionas et al. 2009).

Figure 9 shows the magnetic field structure function for the three spherical shells. Here the spectra across most radii show a slope of  $S_2 \sim l^0$ , with a microscale turnover at roughly 60 kpc. As per the magnetic energy plots in Figure 3, the relaxed clusters have more magnetic energy than the unrelaxed clusters. As discussed by Xu et al. (2011), the total magnetic energy is less than the total kinetic energy. This also holds for scale by scale energy partition; unlike saturated small-scale dynamo (SSD) predictions, there is no scale below which magnetic energy is in equipartition with the kinetic energy at any radius.

### 3.3.2. Spectral Energy Transfer Functions

Spectral energy transfer analysis was a technique developed by Kraichnan (1967) to probe the methods by which energy transfer occurs between energy reservoirs, and is one of the most direct methods for examining the amplification and dissipation processes acting on the magnetic field. A power spectrum of the form  $E(k)$  describes the total energy distribution as a function of wave number, or spatial scale, whereas a transfer function spectrum shows the total transfer of energy into or out of scale  $k$  of some energy reservoir due to a force-mediated interaction with another reservoir. We give a detailed derivation of the transfer function values in the Appendix. This closely follows the approach of Pietarila Graham et al. (2010), but is extended to include self-gravitation.

In general the transfer functions are denoted  $T_{XYZ}(k)$ , which indicates transfer from energy reservoir  $X$ , to scale  $k$  of reservoir  $Y$ , via force  $Z$ . In this analysis, the source reservoir is integrated over all wavenumbers, while the destination is at a specific wavenumber,  $k$ . The transfer function values are calculated by taking a small ( $100^3$  cells,  $\sim 1$  Mpc), fixed resolution cube at the center of the cluster, taking the appropriate quantities' Fourier transforms and dotting them together accordingly, as per the discussion in the Appendix. We chose to only use this small central box because clusters have strong radial dependence. By using a small cube in the center we approximate an idealized turbulent box.

More specifically, we look at the transfer functions  $T_{KBT}$ ,  $T_{BKT}$ ,  $T_{KBP}$ , and  $T_{BKP}$ .  $T_{KBT}$  (and  $T_{BKT}$ ) measure the transfer of kinetic energy to magnetic energy (and vice versa) due to tension forces. By tension forces we mean energy transfer due to stretching and bending of field lines.  $T_{KBP}$  and  $T_{BKP}$  are the energy transfers due to magnetic pressure and the internal magnetic cascade. In a compressible fluid these two terms cannot be disentangled from each other *a priori*, whereas an incompressible fluid guarantees that  $\nabla \cdot \vec{u} = 0$ , making the transfer all due to internal magnetic cascade (Pietarila Graham et al. 2010).

Figure 10 shows transfer of energy from the kinetic energy reservoir to scale  $k$  of the magnetic energy reservoir due to the tension force. As the values are nearly all positive, every scale of magnetic field has energy being transferred from kinetic energy. Additionally, the magnitude of the normalized energy transfer is very similar across all clusters, relaxed and

unrelaxed. There is one relaxed cluster that has some energy transfer away from the magnetic energy at a scale of around 20 kpc.

Figure 11 is the transfer of energy from the magnetic energy reservoir to scale  $k$  of the kinetic energy. In general, the larger scales of kinetic energy lose energy to magnetic fields. In relaxed clusters and some unrelaxed clusters the smaller scales of kinetic energy take energy from the magnetic field. In other unrelaxed clusters the transfer function is very noisy at smaller scales, indicating that neither transfer direction dominates (i.e., comparable amounts of energy are transferred from magnetic to kinetic energy, and vice versa, at small scales). The turnover between energy transfer from and energy transfer to magnetic fields appears to occur at a slightly larger scale for relaxed clusters than unrelaxed clusters, but the sample size is quite small. In general this happens around 40–60 kpc.

In Figure 12 we show the transfer of kinetic energy to magnetic energy at scale  $k$  via pressure. Generally, the smaller scales of magnetic energy gain energy from the kinetic reservoir via pressure forces, while larger scales of magnetic field show a less regular pattern but tend to lose energy to the kinetic reservoir due to pressure. The point where the behavior changes is widely dispersed between clusters but lies between scales of 50 and 100 kpc.

We also examined the transfer of energy from the magnetic reservoir to the kinetic reservoir at scale  $k$  due to pressure, but found that spectra for all clusters were exceedingly noisy. The magnitude of normalized energy transfer remained the same for all clusters, but oscillated between positive and negative values. This indicates that the energy transfer due to this mechanism is in rough equilibrium and does not have a large impact in the total dynamics of the systems.

Because there is consistent loss of magnetic energy due to pressure at large scales and gain of magnetic energy due to pressure at small scales with no net gain or loss of kinetic energy at any scale, this is consistent with compressible effects being largely negligible and  $T_{KBP}$  being equivalent to the transfer function of the magnetic cascade.

These transfer functions depict a scenario where large scale fluid motion bends the magnetic field at all scales, all scales of the magnetic field do work to induce fluid motion at small scales via magnetic tension, and compressive motions act to cascade energy from larger magnetic field scales to smaller scales. This picture is shown schematically in Figure 13.

*This picture is consistent with a small scale dynamo stuck in the kinematic stage due to a lack of turbulent support at small scales.* Moll et al. (2011) show transfer functions for compressible simulations of small scale dynamo action in both the saturated and kinematic stage, and our results are qualitatively similar to those in the kinematic stage. The magnetic field is not able to grow to the saturated stage due to the energy lost to the kinetic energy reservoir at small scales. As small scale kinetic energy is dissipated by numerical viscosity, there is less small scale turbulent motion to do work against magnetic tension. Thus, the magnetic energy reservoir loses energy stored in tension and is unable to build up and reach a saturated state at small scales.

## 4. DISCUSSION

Flux freezing and small-scale dynamo (SSD) action are two processes that can drive the amplification of magnetic fields in clusters. A completely "frozen in" magnetic field will eventually be mixed across the entire volume due to fluid motion

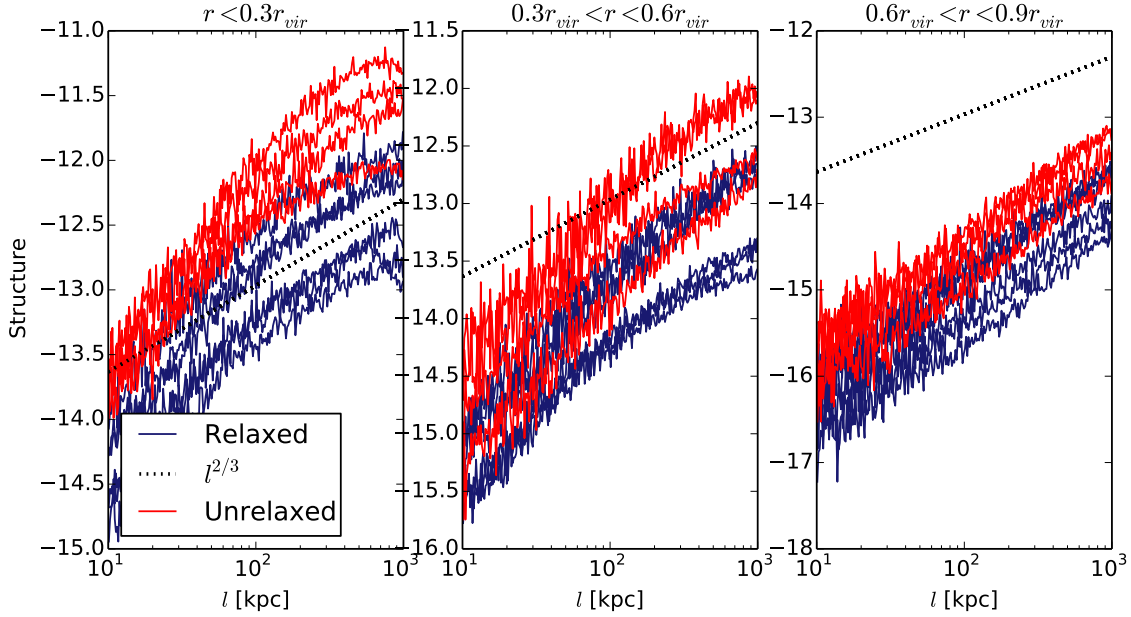


**Figure 8.** Smoothed momentum structure function calculated in spherical shells. Each panel shows one spherical shell with a line corresponding to a single cluster. Blue lines indicate relaxed clusters, while red lines indicate unrelaxed clusters. The dashed line indicates a power law of  $S_2(\rho) \sim l^{4/3}$  and the dotted line indicates a power law of  $S_2(\rho) \sim l^{2/3}$  (Kolmogorov turbulence).

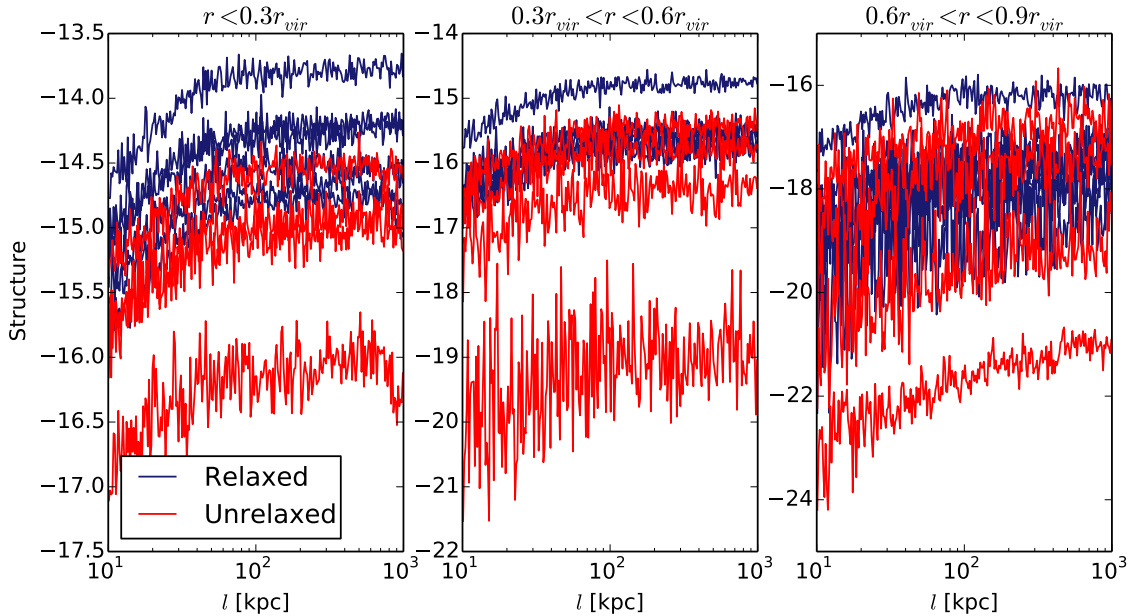


**Figure 9.** Smoothed magnetic field structure function calculated in spherical shells. Each panel shows one spherical shell with a line corresponding to a single cluster. Blue lines indicate relaxed clusters, while red lines indicate unrelaxed clusters.



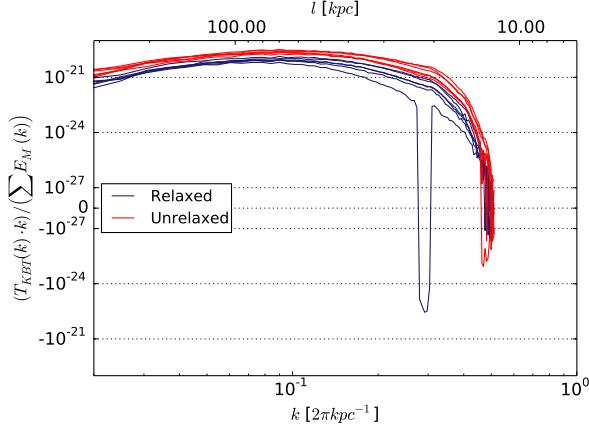


**Figure 10.** Transfer of kinetic energy of all scales to magnetic energy at scale  $k$ , via tension, normalized by magnetic energy. Positive values indicate kinetic energy is transforming to magnetic energy at scale  $k$ , while negative values indicate the magnetic energy at scale  $k$  is losing energy to the kinetic energy reservoir. Relaxed clusters are in *blue* and unrelaxed clusters are in *red*. The large dip is present only in cluster 3.

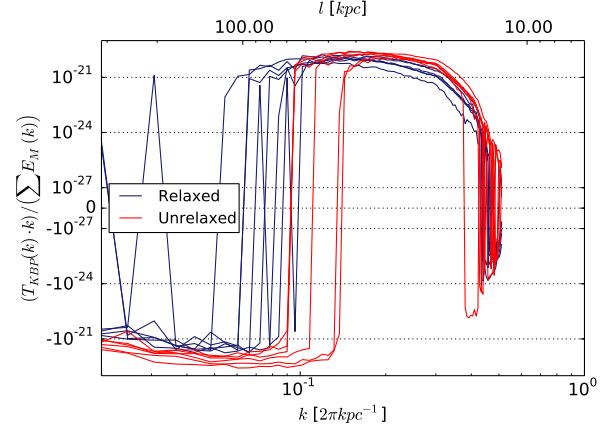


**Figure 12.** Transfer of kinetic energy of all scales to magnetic energy at scale  $k$ , via pressure, normalized by magnetic energy. Positive values indicate kinetic energy is transforming to magnetic energy at scale  $k$ , while negative values indicate the magnetic energy at scale  $k$  is losing energy to the kinetic energy reservoir. Relaxed clusters are in *blue* and unrelaxed clusters are in *red*.

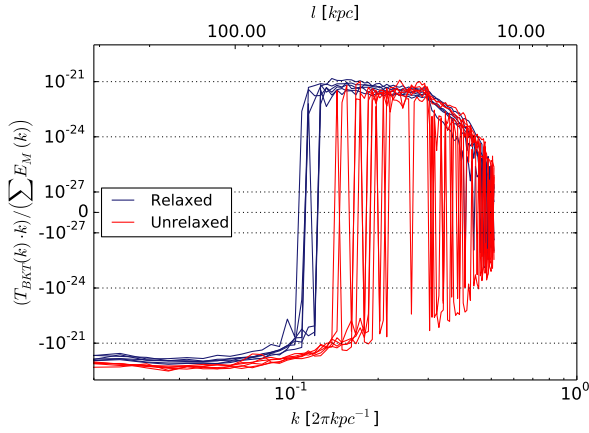


**Figure 11.** Transfer of magnetic energy of all scales to kinetic energy at scale  $k$ , via tension, normalized by magnetic energy. Positive values indicate magnetic energy is transforming to kinetic energy at scale  $k$ , while negative values indicate the kinetic energy at scale  $k$  is losing energy to the magnetic energy reservoir. Relaxed clusters are in *blue* and unrelaxed clusters are in *red*.

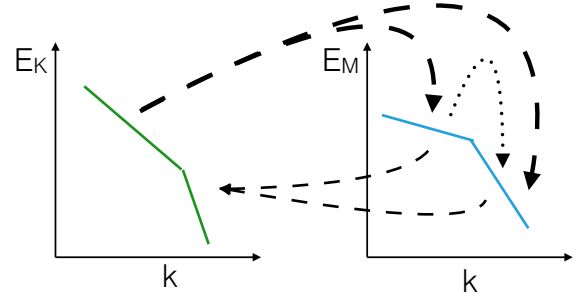


**Figure 13.** Schematic example of the transfer between the kinetic energy reservoir and the magnetic energy reservoir. Dashed lines indicate transfer due to tension and dotted lines indicate transfer due to compression.

dragging the magnetic field. The resulting field will follow a  $B \sim \rho^{2/3}$  power law. SSD action will act to bend and fold a small, random initial magnetic field, quickly amplifying it. When the SSD is saturated the magnetic field energy will be in equipartition with the kinetic energy below some saturation scale, shown schematically in Figure 14.

Both of these processes are active in the real intracluster medium. A high value of  $\beta$  indicates that the magnetic field is dynamically unimportant and thus completely frozen in and thus the field will not impact the flow. A small-scale dynamo will be active for large Reynolds and Prandtl numbers ( $Re \equiv UL/\nu$  and  $Pm \equiv \nu/\eta$ ), both of which the ICM satisfies ( $Re > 10^{12}$ ,  $Pr > 10^{10}$ ).

In simulations like the ones presented in this work, adia-

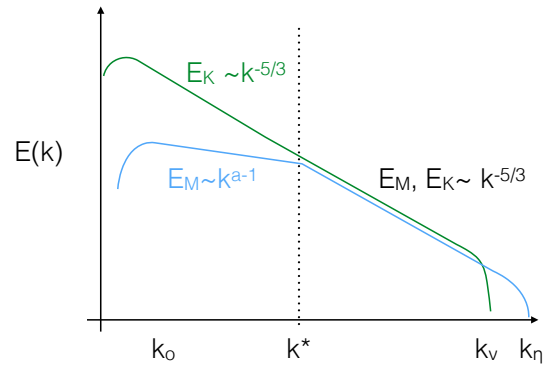


**Figure 14.** Schematic depiction of the magnetic and kinetic power spectra for a small scale dynamo.  $k^*$  denotes the equipartition scale,  $k_\nu$  is the viscous dissipation scale, and  $k_\eta$  is the resistive scale.

batic expansion of the magnetic field from frozen-in field lines occurs, but true nonlinear small-scale dynamo action does not. Plasma  $\beta$  values are very high in all regions of the cluster, across many sizes and relaxation states (as shown in Figure 4). Reynolds numbers and magnetic Reynolds numbers achieved by these simulations, however, are not nearly as high as in the actual ICM (in these calculations,  $Re \sim 1000$ ,  $Pr \sim 1$ ).

The physical regimes where a small-scale dynamo can be active in has been the subject of recent debate. [Haugen et al. \(2004\)](#) find that for  $Pr \sim 1$ , the critical  $R_M \sim 70$ . [Federath et al. \(2011\)](#) find that the Jeans length must be resolved by at least 30 cells to see dynamo action, and without increased resolution most of the amplification will still be due to compressive forces. [Beresnyak \(2012\)](#) show that the transition to a nonlinear dynamo is strongly dependent on the effective Reynolds number; the timescale of the transition from the linear regime to the nonlinear regime is roughly  $t_{linear} \sim t_{dyn} Re^{-1/2}$ , and the magnetic energy growth rate is  $\gamma \sim Re^{1/2}/30\tau_L$ . Thus, for even reasonably large  $Re$ , the magnetic energy at time  $t$  will be greatly reduced from expectations.

From estimates of  $Re$  ( $\sim 1000$ ) and  $\Delta x/\lambda_J$  ( $\sim 30$ ), as well as the structure and transfer function analysis, it is clear that our simulations do not have a nonlinear small-scale dynamo and are likely stuck in the linear phase.

From [Xu et al. \(2011\)](#) we know that major mergers are a critical driver of magnetic field amplification in these clusters. This is likely because the temporary increase in turbulence provides more kinetic energy which is available to be converted to magnetic energy. This transfer likely takes the form of small scale kinetic energy doing work on the magnetic field to increase tension energy at all scales of the magnetic field. Figure 10 shows that only unrelaxed clusters with recent mergers show any net flow from kinetic energy to small scales of magnetic energy. All relaxed clusters have a net flow of small scale magnetic tension energy to the kinetic reservoir.

That the turnover of the magnetic field structure function,  $T_{KBT}$  transfer function and the end of the kinetic energy inertial range all occur at roughly 80 kpc ( $\sim 8\Delta x$ ) is not a coincidence. These metrics are all intertwined and critically depend on the numerical dissipation of the simulations. As [Kitsionas et al. \(2009\)](#) found similar limits to the inertial range due to numerical viscosity across a variety of codes and numerical methods, it is likely that a similar turnover range and magnetic field growth rate will be seen in other simulations.

This picture is likely worse in the outskirts of the cluster. Although the AMR resolution criteria ensure refinement on both overdensity and resistive length, the spatial resolution is poorer, there is no inertial range in the structure function, and there is remarkably little correlation in the magnetic field. Although we cannot do the same transfer function analysis in the outskirts due to the strong density gradients, we expect that the transfer will be nearly entirely due to compressive motions. Even if simulations were able to increase the spatial resolution in the centers of clusters enough to ensure transition to the non-linear regime of dynamo action, the outskirts of the clusters would still lag behind, likely affecting global cluster properties.

Clearly it is not possible to excite ICM level magnetic field growth via small-scale dynamo action in current simulations. Even the highest Reynolds numbers achievable by current generation simulations are orders of magnitude smaller than physically realistic values. Thus, the magnetic growth

timescale will always be far too small. Increasing the simulation spatial resolution enough to diminish the effects of numerical viscosity is computationally unfeasible, so alternative models must be considered. [Beresnyak & Miniati \(2016\)](#) consider a model where time-dependent global cluster turbulence analysis is used to derive the turbulent dissipation rate  $\epsilon_{turb}$ , which then constrains the possible magnetic energy density. Another possible approach could be to use a subgrid turbulence model, similar to that of [Scannapieco & Brüggel \(2008\)](#), to add additional turbulent support and counteract the effects of numerical viscosity. Regardless, in order to study any process dependent on cluster magnetic fields, a model that is more sophisticated than the current cosmological MHD simulations must be utilized.

## 5. SUMMARY

In this paper we have further analyzed a set of 12 cosmological magnetohydrodynamic AMR simulations of galaxy clusters, originally presented by [Xu et al. \(2009, 2010, 2011, 2012\)](#). The goal of this effort is to characterize the nature of the magnetized intracluster plasma in order to inform more accurate plasma simulations, thus guiding the creation of sub-grid models for plasma behavior that can be applied to cosmological simulations. Our primary results are as follows:

1. Although both flux-freezing and small-scale dynamo play a role in the amplification of the magnetic field, most field amplification is due to the compressive modes associated with flux-freezing.
2. Small-scale dynamo action is limited due to the low effective Reynolds number of the ICM, which is small because of numerical viscosity. This limits the inertial range of the kinetic turbulent cascade, reducing the turbulent energy available to do work on the magnetic field.
3. This picture is applicable across a variety of cluster relaxation states; although there is an increase in turbulence associated with major mergers, it is not enough to boost the small-scale dynamo out of the kinematic stage. Unrelaxed clusters show more energy transfer from small scales of kinetic energy to magnetic energy than relaxed clusters, but it is only associated with a moderate increase in magnetic field amplification.
4. We see even less small-scale dynamo action in the outskirts of clusters as in the central region. As the spatial resolution is poorer in the outskirts of the cluster, the Reynolds number is even higher, making the timescale of the linear dynamo even longer.
5. Due to the similarity in the small-scale behavior of turbulent cascades across a variety of astrophysical fluid codes ([Kitsionas et al. 2009](#)) and the strong dependence of small-scale dynamo action on cluster turbulence ([Xu et al. 2011](#)), we expect these results to be similar across a variety of simulation codes.

## 6. ACKNOWLEDGMENTS

The authors would like to thank Kris Beckwith, Andrew Christlieb, Jeff Oishi, and Mark Voit for helpful discussions during the preparation of this paper. This work was supported

by NASA through grants NNX12AC98G, NNX15AP39G, Hubble Theory Grants HST-AR-13261.01-A and HST-AR-14315.001-A, and by the DOE Computational Science Graduate Fellowship program. The simulations presented in this paper were performed on LANL supercomputing resources, and analyzed on the TACC Stampede supercomputer under XSEDE allocations TG-AST090040 and TG-AST100004. This work was supported in part by Michigan State University through computational resources provided by the Institute for Cyber-Enabled Research. BWO was supported in part by the sabbatical visitor program at the Michigan Institute for Research in Astrophysics (MIRA) at the University of Michigan in Ann Arbor, and gratefully acknowledges their hospitality. This work was also supported by grants to J.O.B. from the National Science Foundation (AST 1106437) and from NASA (NNX15AE17G). HL gratefully acknowledges the support by LANL's LDRD program and DoE/OFES through CMSO. `Enzo` and `yt` are developed by a large number of independent researchers from numerous institutions around the world. Their commitment to open science has helped make this work possible.

## REFERENCES

- Beresnyak, A. 2012, *Physical Review Letters*, 108, 035002  
 Beresnyak, A., & Miniati, F. 2016, *ApJ*, 817, 127  
 Bonafede, A., Feretti, L., Murgia, M., Govoni, F., Giovannini, G., Dallacasa, D., Dolag, K., & Taylor, G. B. 2010a, *A&A*, 513, A30  
 Bonafede, A., Feretti, L., Murgia, M., Govoni, F., Giovannini, G., & Vacca, V. 2010b, *ArXiv e-prints*  
 Borgani, S., & Kravtsov, A. 2009, *ArXiv* 0906.4370  
 Brandenburg, A., & Subramanian, K. 2005, *Physics Reports*, 417, 1  
 Brüggén, M., Scannapieco, E., & Heinz, S. 2009, *MNRAS*, 395, 2210  
 Bryan, G. L., et al. 2014, *ApJS*, 211, 19  
 Burns, J. O., Skillman, S. W., & O'Shea, B. W. 2010, *ApJ*, 721, 1105  
 Burns, J. O., Sulkanen, M. E., Gisler, G. R., & Perley, R. A. 1992, *ApJL*, 388, L49  
 Carilli, C. L., & Taylor, G. B. 2002, *ARA&A*, 40, 319  
 Clarke, T. E., & Ensslin, T. A. 2006, *AJ*, 131, 2900  
 Collins, D. C., Xu, H., Norman, M. L., Li, H., & Li, S. 2010, *The Astrophysical Journal Supplement Series*, 186, 308  
 Datta, A., Schenck, D. E., Burns, J. O., Skillman, S. W., & Hallman, E. J. 2014, *ApJ*, 793, 80  
 Federrath, C., Sur, S., Schleicher, D. R. G., Banerjee, R., & Klessen, R. S. 2011, *ApJ*, 731, 62  
 Feretti, L., Dallacasa, D., Giovannini, G., & Tagliani, A. 1995, *A&A*, 302, 680  
 Fromang, S., & Papaloizou, J. 2007, *A&A*, 476, 1113  
 Giacintucci, S., Venturi, T., Cassano, R., Dallacasa, D., & Brunetti, G. 2009, *ApJL*, 704, L54  
 Hallman, E. J., Motl, P. M., Burns, J. O., & Norman, M. L. 2006, *ApJ*, 648, 852  
 Haugen, N. E. L., Brandenburg, A., & Mee, A. J. 2004, *MNRAS*, 353, 947  
 Kitsionas, S., et al. 2009, *A&A*, 508, 541  
 Kraichnan, R. H. 1967, *Physics of Fluids*, 10, 1417  
 Kritsuk, A. G., Norman, M. L., Padoan, P., & Wagner, R. 2007, *ApJ*, 665, 416  
 Lawler, J. M., & Dennison, B. 1982, *ApJ*, 252, 81  
 Li, H., Lapenta, G., Finn, J. M., Li, S., & Colgate, S. A. 2006, *ApJ*, 643, 92  
 Markevitch, M., & Vikhlinin, A. 2007, *Physics Reports*, 443, 1  
 Miniati, F. 2014, *ApJ*, 782, 21  
 —. 2015, *ApJ*, 800, 60  
 Moll, R., Pietarila Graham, J., Pratt, J., Cameron, R. H., Müller, W.-C., & Schüssler, M. 2011, *ApJ*, 736, 36  
 Murgia, M., Govoni, F., Feretti, L., Giovannini, G., Dallacasa, D., Fanti, R., Taylor, G. B., & Dolag, K. 2004, *A&A*, 424, 429  
 Nagai, D. 2006, *ApJ*, 650, 538  
 Pietarila Graham, J., Cameron, R., & Schüssler, M. 2010, *ApJ*, 714, 1606  
 Scannapieco, E., & Brüggén, M. 2008, *ApJ*, 686, 927  
 Simon, J. B., Hawley, J. F., & Beckwith, K. 2009, *ApJ*, 690, 974  
 Skillman, S. W., Xu, H., Hallman, E. J., O'Shea, B. W., Burns, J. O., Li, H., Collins, D. C., & Norman, M. L. 2013, *ApJ*, 765, 21  
 Skory, S., Hallman, E., Burns, J. O., Skillman, S. W., O'Shea, B. W., & Smith, B. D. 2013, *ApJ*, 763, 38  
 Smith, B., O'Shea, B. W., Voit, G. M., Ventimiglia, D., & Skillman, S. W. 2013, *ApJ*, 778, 152  
 Subramanian, K., Shukurov, A., & Haugen, N. E. L. 2006, *MNRAS*, 366, 1437  
 Turk, M. J., Smith, B. D., Oishi, J. S., Skory, S., Skillman, S. W., Abel, T., & Norman, M. L. 2011, *ApJS*, 192, 9  
 van Weeren, R. J., Röttgering, H. J. A., Brüggén, M., & Hoeft, M. 2010, *Science*, 330, 347  
 Vikhlinin, A. A., & Markevitch, M. L. 2002, *Astronomy Letters*, 28, 495  
 Voit, G. M. 2005, *Reviews of Modern Physics*, 77, 207  
 Werner, N., et al. 2015, *ArXiv e-prints*  
 Xu, H., Li, H., Collins, D., Li, S., & Norman, M. L. 2008, *ApJL*, 681, L61  
 Xu, H., Li, H., Collins, D. C., Li, S., & Norman, M. L. 2009, *ApJL*, 698, L14  
 —. 2010, *ApJ*, 725, 2152  
 —. 2011, *ApJ*, 739, 77  
 Xu, H., et al. 2012, *ApJ*, 759, 40  
 Zuhone, J. A., Kunz, M. W., Markevitch, M., Stone, J. M., & Biffi, V. 2015, *ApJ*, 798, 90

## APPENDIX

Spectral energy transfer functions were initially developed in the incompressible limit by Kraichnan (1967). It was later extended to include the compressible limit (Fromang & Papaloizou 2007; Simon et al. 2009; Pietarila Graham et al. 2010). Here we follow closely the approach of Pietarila Graham et al. (2010) but extend the framework to include a self-gravitating fluid.

A galaxy cluster is a strongly stratified environment that is not generally periodic, so we continue using a general orthonormal basis  $\phi_k(\mathbf{x})$  and arbitrary function  $g(\mathbf{x})$ . Then our test function  $g(\mathbf{x})$  can be written in k-space as

$$\hat{g}(k) = \int_{\Omega} g(\mathbf{x}) \phi_k(\mathbf{x}) d^3x \quad (1)$$

with

$$g(\mathbf{x}) = \sum_k \hat{g}(k) \phi_k(\mathbf{x}) \quad (2)$$

where  $\Omega$  is the analysis volume.  $\hat{g}(k)$  is then the spectral density of some global quantity  $G$  in k-space, where  $G$  is

$$G = \int_{\Omega} g(\mathbf{x}) d^3x = \sum_k \hat{g}(k). \quad (3)$$

In real space the magnetic energy density can be written as  $e_M = \frac{1}{8\pi} |B|^2$ . The total magnetic energy is

$$E_M = \int_{\Omega} e_M dx^3 = \sum_k E_M(k) \quad (4)$$

so Parseval's theorem allows us to write the spectral energy density as

$$E_M(k) = \frac{1}{8\pi} \widehat{\mathbf{B}}(k) \cdot \widehat{\mathbf{B}}^*(k). \quad (5)$$

Similarly, the momentum energy density can be written  $e_K = \frac{1}{2} \rho u^2$ , so the real kinetic spectral energy density can be written as

$$E_K(k) = \frac{1}{4} \left( \widehat{\mathbf{u}}(k) \cdot [\widehat{\rho \mathbf{u}}]^*(k) + [\widehat{\rho \mathbf{u}}](k) \cdot \widehat{\mathbf{u}}^*(k) \right) \quad (6)$$

To break up the spectral energy densities into their components we write the magnetic induction equation

$$\frac{\partial \mathbf{B}}{\partial t} = \nabla \times (\mathbf{u} \times \mathbf{B}) \quad (7)$$

and the conservative form of the momentum equation

$$\frac{\partial(\rho \mathbf{u})}{\partial t} + \nabla \cdot (\rho \mathbf{u} \mathbf{u}) = -\nabla P + (\nabla \times \mathbf{B}) \times \mathbf{B} - \rho \nabla \phi \quad (8)$$

with  $P$  as the thermal pressure and  $\phi$  as the gravitational potential. Combining the conservative form of the momentum equation with the continuity equation

$$\frac{\partial \rho}{\partial t} + \nabla \cdot (\rho \mathbf{u}) = 0 \quad (9)$$

allows us to write the momentum equation in terms of velocity

$$\frac{\partial \mathbf{u}}{\partial t} = -(\mathbf{u} \cdot \nabla) \mathbf{u} - \frac{1}{\rho} \nabla P + \frac{1}{\rho} (\nabla \times \mathbf{B}) \times \mathbf{B} - \nabla \phi. \quad (10)$$

The time evolution of the spectral magnetic energy can be written

$$\frac{dE_M(k)}{dt} = \frac{1}{4\pi} \text{Re} \left[ \frac{\partial \widehat{\mathbf{B}}}{\partial t} \cdot \widehat{\mathbf{B}}^* \right] \quad (11)$$

so its component form can be derived by projecting the induction equation (Equation 7) onto its basis components in k-space, dotting it with  $\frac{1}{4\pi} \widehat{\mathbf{B}}^*(k)$ , and taking the real component to obtain

$$\frac{d}{dt} E_M(k) = T_{KBP} + T_{KBT} + D_B \quad (12)$$

where

$$T_{KBT} = \frac{1}{4\pi} \text{Re} \left[ \widehat{\mathbf{B}}(k) \cdot [\widehat{\mathbf{B}} \cdot \nabla \mathbf{u}]^*(k) \right] \quad (13)$$

represents the energy transfer rate from the kinetic energy reservoir to the magnetic energy reservoir due to magnetic tension,

$$T_{KBP} = \frac{1}{4\pi} \text{Re} \left[ \widehat{\mathbf{B}}(k) \cdot [\widehat{\mathbf{B}} \nabla \cdot \mathbf{u}]^*(k) - \widehat{\mathbf{B}} \cdot [\widehat{\mathbf{u}} \cdot \nabla \widehat{\mathbf{B}}]^*(k) \right] \quad (14)$$

represents the energy transfer rate from the kinetic reservoir to the magnetic reservoir due to magnetic pressure, and  $D_B$  is the dissipation due to numerical resistivity.

Similarly, the time evolution of the spectral kinetic energy can be written as

$$\frac{d}{dt} E_K(k) = \frac{1}{2} \text{Re} \left[ \widehat{\mathbf{u}}(k) \cdot \frac{\partial [\widehat{\rho \mathbf{u}}]^*(k)}{\partial t} + \frac{\partial \widehat{\mathbf{u}}(k)}{\partial t} \cdot [\widehat{\rho \mathbf{u}}]^*(k) \right] \quad (15)$$

so to break it into its components the conservative form of the momentum equation (Equation 8) and the primitive form of the momentum equation (Equation 10) are projected onto their basis components and dotted with the appropriate vectors to find

$$\frac{dE_K(k)}{dt} = T_{KKA}(k) + T_{KKC}(k) + T_{BK}(k) + T_{IK} + D_K \quad (16)$$

Here,

$$T_{KKA}(k) = -\frac{1}{2} \text{Re} \left[ \widehat{\mathbf{u}} \cdot [\widehat{\mathbf{u}} \cdot \nabla(\rho \mathbf{u})]^* (\mathbf{k}) + [\widehat{\rho \mathbf{u}}]^* (\mathbf{k}) \cdot [\widehat{\mathbf{u}} \cdot \nabla \mathbf{u}] (\mathbf{k}) \right] \quad (17)$$

is the transfer of kinetic energy inside the kinetic energy reservoir due to advection,

$$T_{KKC}(k) = -\frac{1}{2} \text{Re} \left[ \widehat{\mathbf{u}} \cdot [\widehat{\rho \mathbf{u}} \nabla \cdot \mathbf{u}]^* (\mathbf{k}) \right] \quad (18)$$

is the transfer of kinetic energy inside the kinetic reservoir due to compressible motion,

$$T_{BKT} = \frac{1}{8\pi} \text{Re} \left[ \widehat{\mathbf{u}} \cdot [\widehat{\mathbf{B}} \cdot \nabla \mathbf{B}]^* (\mathbf{k}) + [\widehat{\rho \mathbf{u}}]^* (\mathbf{k}) \cdot \left[ \frac{1}{\rho} \widehat{\mathbf{B}} \cdot \nabla \mathbf{B} \right] (\mathbf{k}) \right] \quad (19)$$

is the transfer of energy from the magnetic energy reservoir due to magnetic tension, and

$$T_{BKP} = \frac{1}{8\pi} \text{Re} \left[ \widehat{\mathbf{u}} (\mathbf{k}) \cdot \left[ -\frac{1}{2} \widehat{\nabla |\mathbf{B}|^2} \right]^* (\mathbf{k}) + [\widehat{\rho \mathbf{u}}]^* (\mathbf{k}) \cdot \left[ -\frac{1}{2\rho} \widehat{\nabla |\mathbf{B}|^2} \right] (\mathbf{k}) \right] \quad (20)$$

is the transfer of magnetic energy to kinetic energy due to pressure.